A tetrahedral-based superconvergent scheme for aeroacoustics

Nicolas Gourvitch, Gilbert Rogé, Ilia Abalakin, Alain Dervieux, Tatiana Kozubskaya

INRIA

INSTITUT NATIONAL DE RECHERCHE EN INFORMATIQUE ET EN AUTOMATIQUE

A tetrahedral-based superconvergent scheme for aeroacoustics

N. Gourvitch, G. Rogé, I. Abalakin, A. Dervieux, T. Kozubskaya

N° 5212

May 26, 2004

Thème NUM

ISSN 0249-6399 ISRN INRIA/RR--5212--FR+ENG

INRIA
SOPHIA ANTIPOLIS

A tetrahedral-based superconvergent scheme for aeroacoustics

N. Gourvitch*, G. Rogé†, I. Abalakin‡, A. Dervieux§, T. Kozubskaya¶

Thème NUM — Systèmes numériques
Projet Smash

Rapport de recherche n° 5212 — May 26, 2004 — 28 pages

Abstract: We describe a numerical scheme for hyperbolics well adapted to both aerodynamics and aeroacoustics. The scheme is vertex centered, It applies with second order accuracy to unstructured tetrahedrizations and extends to higher order (up to sixth) on a certain type of cartesian meshes. Several basic aeroacoustic numerical experiments are presented.

Key-words: Aeroacoustics, numerical schemes, hyperbolic models, linearised Euler equations, unstructured meshes

* ENPC, 6-7 avenue B. Pascal, 77455 Champs-sur-Marne, France
† Dassault-Aviation, 78 Quai Marcel Dassault, 92214 Saint-Cloud, France
‡ IMM, Miuskaya sq., 4a, Moscow 125047, Russia
§ INRIA, 2004 Route des Lucioles, BP. 93, 06902 Sophia-Antipolis, France
¶ IMM, Miuskaya sq., 4a, Moscow 125047, Russia

Unité de recherche INRIA Sophia Antipolis
2004, route des Lucioles, BP 93, 06902 Sophia Antipolis Cedex (France)
Téléphone : +33 4 92 38 77 77 — Télécopie : +33 4 92 38 77 65

Un schéma en tétraèdres superconvergent pour l'aéroacoustique

Résumé : Ce rapport décrit un schéma numérique bien adapté à l'aérodynamique et à l'aéroacoustique. Ce schéma est centré sommet et précis au second ordre sur des tetraédrisations non-structurées et d'un ordre plus élevé (jusqu'à six) sur un certain type de tétraédrisation cartésienne. Quelques expérences numériques de base en aéroacoustique sont présentées.

Mots-clés : Aéroacoustique, schémas numériques, modèles hyperboliques, Euler linéarisé, maillages non-structurés

1 Introduction

This paper takes place into a research programme aiming at proposing numerical schemes enough adapted to both acoustic models and comperssible fluid models.
It is in connection to a series of works focusing on the numerical simulation of turbulent flows with second-order schemes applying on unstructured meshes, equipped with a very low dissipative term, see [22],[20],[21].
The numerical simulation of the propagation of acoustic waves with first-order partial differential equations of hyperbolic type has an important impact on aircraft design, [19], and involves a difficult approximation problem. Rather simple second-order accurate methods have been much used and appreciated for elliptic problems. In contrast, for first-order hyperbolics, not only the derivation of genuinely second order methods has costed a lot of efforts, but also it seems that most of second-order methods (and even most of third-order ones) are too dissipative to allow efficient enough accurate computations of acoustics for real life problems.
Several good high order schemes are now available for regular meshes (see, for example, [1]). They are derived from schemes with low dissipation, at least fourth-order accurate, or with a dissipation not larger than the dissipation applied in fourth-order accurate schemes.
The case of regular meshes is a relatively easier one. We can understand this if we consider the simplified case of advection with constant velocity. In that case, finding a good advection scheme is essentially finding an interpolation scheme. In the case of a Courant number equal to 1., some schemes can even be exact. Further, regular meshes are particularly favourable to the derivation of high-order accurate schemes that cost a rather small number of operations for their assembly.
The case of unstructured meshes represents the maximal difficulty. First, mesh irregularity amplifies dispersion phenomena. Secondly, many useful numerical methods do not extend easily (traditional compact schemes, for example) to the "unstructured" case. Today essentially two families of schemes enjoy high-order of accuracy, conservation properties and dissipation ones, the adaptation of ENO-type schemes to unstructured meshes ([2]), and the Discontinuous-Galerkin method ([3]). But these two families of schemes are accurate enough only if they are of fourth order. In that last case, they consume a large computing effort for each unknown, and they are efficient only when enough nodes are used and a very small error is demanded.
From these remarks we can derive the following recommandations for unstructured meshes:
- (i) build second-order schemes that involve as few dissipation as do high-order schemes,
- (ii) equip the second-order scheme of superconvergence properties on cartesian meshes and use as often as possible cartesian meshing of subregions of the computational domain.
By superconvergence properties we mean that the scheme applies to arbitrary unstructured meshes but in region where the mesh is cartesian, the truncation error is smaller by several orders of magnitude. As far as (i) is concerned, we emphasize that the task is complex. Indeed, dissipation should offer a compensation to dispersion in the sense that excessively dispersed high frequencies should be damped in order to avoid oscillations and large errors. The balance is generally obtained by choosing high-order accuracy. However, in the deriva-

tion of the Dispersion Relation Preserving (DRP) scheme, Tam and co-workers prefer to optimize the scheme for low phase error better than keeping accuracy ([1]).

In [11], a family of vertex-centered upwind aeroacoustic schemes applying to tetrahedrizations and presenting superconvergence properties was introduced. This scheme is also used in several works ([18][17][14][15]) The present report proposes a 3D extension of it.

It will have the following properties:
(i) the scheme is conservative,
(ii) the dissipation, when used, is derived from sixth-order derivatives,
(iii) the scheme is fifth-order with dissipation and sixth-order accurate without dissipation when it is applied to a particular cartesian mesh.

2 Low dissipation advection schemes : 1D

Upwind schemes of Godunov type enjoy a lot of interesting qualities due to the perfect adequation of the upwinding mechanism they involve with unsteady waves. Unfortunately, the amount of dissipation they contain seems much larger than necessary for an accurate non-oscillatory numerical answer. As a consequence, the dominant term of the numerical error is carried by the dissipation.

We suggest to forget about strict monotony and to get inspired by Direct Simulation techniques in which non-dissipative high order approximations are stabilised in good accuracy conditions thanks to filters which rely on very-high even order derivatives. We shall first show how this can be done with a one-dimensional high-order MUSCL method modified in such a manner that the dominant dissipation term is a sixth-order derivative. In the linear case, this is exactly the construction of [4] also used in [5].

2.1 Spatial 1D MUSCL formulation

Let us first consider the the one-dimensional convection equation

$$u_t + c\,u_x = 0 \tag{1}$$

The finite-volume method is used for the spatial approximation. x_j , $1 \leq j \leq N$ denote the discretization points of the mesh. For each discretization point, we state : $u_j \approx u(x_j)$ and we define the control volume C_j as the interval $[x_{j-\frac{1}{2}}, x_{j+\frac{1}{2}}]$ where $x_{j+\frac{1}{2}} = \dfrac{x_j + x_{j+1}}{2}$.

Let $U = \{u_j\}$ the unknown vector whose components are approximating the function $u(x)$ in each node j of the mesh. We build the vector $\Psi(U)$ according to spatial approximation of $(f(u))_x$, which can be written as :

$$\Psi_j(U) = \frac{1}{\Delta x}(\Phi_{j+\frac{1}{2}} - \Phi_{j-\frac{1}{2}}) \;;\; \Phi_{j+\frac{1}{2}} = \Phi(u_{j+\frac{1}{2}-}, u_{j+\frac{1}{2}+}) \tag{2}$$

Schemes	δ	β	θ^c	θ^d	**Order**
1	1	1/3	0	0	3
2	1	1/3	- 1/6	0	4
3	1	1/3	0	- 1/6	4
4	1	1/3	- 1/10	- 1/15	5
4	0	1/3	- 1/10	- 1/15	6

Table 1: Accuracy of different versions of the new scheme in 1D case

where $u_{j\pm\frac{1}{2}\pm}$ denote the values of u at boundaries of control volume C_j with $\Phi(u,v) = \frac{c}{2}\left[(1-\delta sign(c))u + (1-\delta sign(c))v\right]$.

According to the MUSCL methodology ([6]), the left and right control volume boundary states $u_{j\pm\frac{1}{2}\pm}$ is built using linear interpolation formulas :

$$\begin{array}{lll} u_{j+\frac{1}{2}-} = u_j + \frac{1}{2}\Delta u_{j+\frac{1}{2}-} & ; & u_{j+\frac{1}{2}+} = u_{j+1} - \frac{1}{2}\Delta u_{j+\frac{1}{2}+} \\ u_{j-\frac{1}{2}-} = u_{j-1} + \frac{1}{2}\Delta u_{j-\frac{1}{2}-} & ; & u_{j-\frac{1}{2}+} = u_j - \frac{1}{2}\Delta u_{j-\frac{1}{2}+} \end{array} \tag{3}$$

where $\Delta u_{j\pm\frac{1}{2}\pm}$ are slopes, i.e. approximations of derivative term $\dfrac{\partial u}{\partial x}$.

$$\Delta u_{j+\frac{1}{2}-} = (1-\beta)(u_{j+1}-u_j) + \beta(u_j - u_{j-1}) \tag{4}$$

$$\Delta u_{j+\frac{1}{2}+} = (1-\beta)(u_{j+1}-u_j) + \beta(u_{j+2} - u_{j+1}) \tag{5}$$

where β,is upwinding parameter that controls the combination of fully upwind and centered slopes. For $\beta = 1/3$ the scheme is the standard third order accurate scheme.
In the present vertex-centered context, high order accuracy is not obtained by a higher-order interpolation but by an interpolation that compensates the error coming from the final central differencing in (2). This writes as follows:

$$\begin{aligned} \Delta u_{j+\frac{1}{2}-} = {} & (1-\beta)(u_{j+1}-u_j) + \beta(u_j - u_{j-1}) \\ & + \theta^c(-u_{j-1} + 3u_j - 3u_{j+1} + u_{j+2}) \\ & + \theta^d(-u_{j-2} + 3u_{j-1} - 3u_j + u_{j+1}) \end{aligned} \tag{6}$$

$$\begin{aligned} \Delta u_{j+\frac{1}{2}+} = {} & (1-\beta)(u_{j+1}-u_j) + \beta(u_{j+2} - u_{j+1}) \\ & + \theta^c(-u_{j-1} + 3u_j - 3u_{j+1} + u_{j+2}) \\ & + \theta^d(-u_j + 3u_{j+1} - 3u_{j+2} + u_{j+3}) \end{aligned} \tag{7}$$

where β, θ^c and θ^d are upwinding parameters that control the combination of fully upwind and centered slopes.

We observe that schemes described in (5) are in general second-order accurate but they become high-order accurate for some values of the parameters β, δ, θ^c and θ^d. We note that for $\theta^c = 0$, $\theta_d = -1/6$ we maximise the degree of upwinding. Also, fifth order accuracy

β	θ^c	θ^d	CFL_{max}
1/3	0	0	2.310
1/3	- 1/6	0	0.263
1/3	0	- 1/6	1.332
1/3	- 1/10	- 1/15	1.867

Table 2: Maximal Courant numbers (explicit RK6 scheme) for the four different spatial schemes (1D analysis)

is obtained with an adequate choice of the three coefficients. For this last case, but with $\delta = 0$, then we get a central-differenced sixth-order accurate scheme.

2.2 Time advancing stability

We can combine the above scheme with the standard Runge-Kutta time advancing.

Since the purpose is to compute linear acoustics, we can simplify the Runge-Kutta scheme to the linearised Jameson variant ([7]) which writes as follows:

$$\begin{aligned} &U^{(0)} = U^n \\ &U^{(k)} = U^{(0)} + \frac{\Delta t}{N-k+1} L\left(U^{(k-1)}\right), \quad k = 1 \dots N \\ &U^{n+1} = U^{(N)} \end{aligned} \tag{8}$$

We recall in Table 2 some typical maximal CFL numbers for the six-stage RK scheme, which ensure a global accuracy of five for the two best schemes of the proposed family. This table illustrates that the above schemes can be used with CFL number of the order of the unity.

3 Unstructured two-dimensional case

The family of 2D schemes that is considered is a *mixed finite-volume finite-element approximation*, applying on triangulations, and of *vertex-centered* type. We refer to [8] for a detailed description of this family of scheme.

Around each vertex is built a cell following to main options:
- either the cell is limited by part of the medians of surrounding triangles,
- or the cell is built according to an idea of Barth ([9]) by joining the center of edges with the center of smallest circle containing the considered triangle.

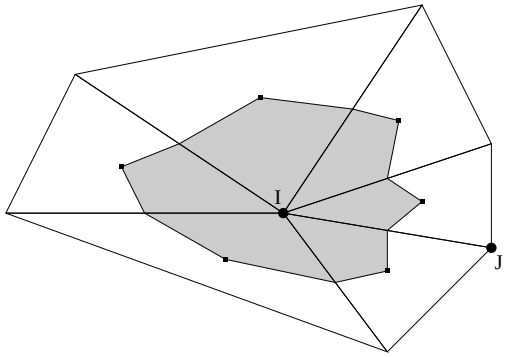

Figure 1: Median cell construction

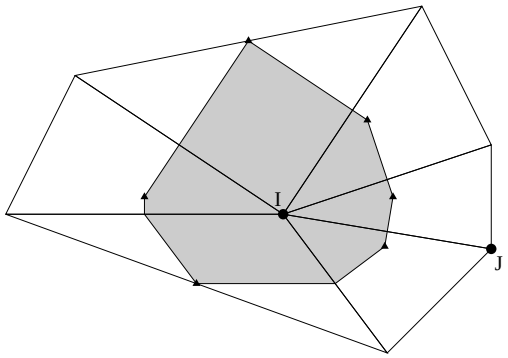

Figure 2: Circumcenter "Barth" cell construction

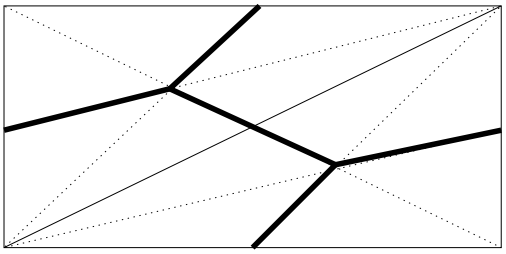

Figure 3: Trace of the medians division on two Friedrichs-Keller elements

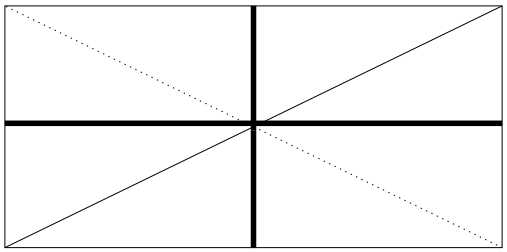

Figure 4: Trace of Barth division on two Friedrichs-Keller elements

The fluxes are assembled on an edge-based process, i.e. for each edge ij between two nodes i and j, and then summed for each node i as follows:

$$area_i \; W_{i,t} \quad F \quad + \Sigma \;\; \Phi_{ij} \quad = \quad 0 \tag{9}$$

where Φ_{ij} are elementary fluxes computed with Riemann solvers.
We first recall the features of an extended version proposed in [4], [5] for Euler calculations.

The numerical integration with an upwind scheme generally leads to approximations which are only first-order accurate. The MUSCL methodology of van Leer has been extended to vertex-centered unstructured formulations in order to reach second order accuracy (see for example [8]). This extension relies on the evaluation fluxes with extrapolated values W_{ij}, W_{ji} at the interface of the cells (Figure 5): with:

$$\left\{ \begin{array}{rcrcl} W_{ij} & = & W_i & + & 0.5 \; (\vec{\nabla} W)_{ij}.\vec{ij} \\ W_{ji} & = & W_j & - & 0.5 \; (\vec{\nabla} W)_{ji}.\vec{ij} \end{array} \right. \tag{10}$$

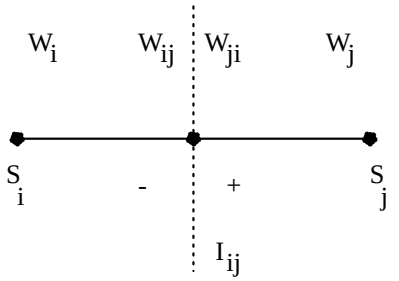

Figure 5: Position of W_{ij} and W_{ji} on $[S_i,S_j]$

where the "extrapolation slopes" $(\vec{\nabla} W)_{ij,ji}$ are obtained using a combination of centered and upwind gradients.

In order to increase the accuracy of the basic MUSCL construction, we propose to define these slopes as follows :
The centered gradient $(\vec{\nabla} W)^c_{ij}$ is defined as $(\vec{\nabla} W)^c_{ij} . \vec{ij} = W_j - W_i$.
The nodal gradient $(\vec{\nabla} W)_i$ is calculated on the cell C_i as the average of the gradients of the triangles which include the considered node :

$$(\vec{\nabla} W)_i = \frac{1}{aire(C_i)} \sum_{T \in C_i} \frac{aire(T)}{3} \sum_{k \in T} W_k \vec{\nabla} \Phi^T_k \tag{11}$$

The upwind gradient is computed according to the definition of the downstream and upstream triangles which can be associated with an edge $[S_i\, S_j]$ (Figure 6). The downstream and upstream triangles are respectively noted T_{ij} and T_{ji}. One has so :
$(\vec{\nabla} W)^d_{ij} = \vec{\nabla} W|_{T_{ij}}$ and $(\vec{\nabla} W)^u_{ij} = \vec{\nabla} W|_{T_{ji}}$ where $\vec{\nabla} W|_T = \sum_{k \in T} W_k \vec{\nabla} \Phi_k|_T$ are the P1-Galerkin gradients on triangle T. This option allows extensions to Local Extremum Diminishing (LED) schemes as shown in [7].

We now specify our method for computing the extrapolation slopes $(\vec{\nabla} W)_{ij}$ and $(\vec{\nabla} W)_{ji}$:

$$\begin{aligned} (\vec{\nabla} W)_{ij}.\vec{ij} = \quad & (1-\beta)(\vec{\nabla} W)^c_{ij}.\vec{ij} + \beta(\vec{\nabla} W)^u_{ij}.\vec{ij} \\ & + \xi_c \left[(\vec{\nabla} W)^u_{ij}.\vec{ij} - 2(\vec{\nabla} W)^c_{ij}.\vec{ij} + (\vec{\nabla} W)^d_{ij}.\vec{ij} \right] \\ & + \xi_d \left[(\vec{\nabla} W)_{D^*_{ij}}.\vec{ij} - 2(\vec{\nabla} W)_i.\vec{ij} + (\vec{\nabla} W)_j.\vec{ij} \right] \quad , \end{aligned} \tag{12}$$

The computation of W_{ji} is analogous:

$$\begin{aligned}(\vec{\nabla}W)_{ji}.\vec{ij} = \quad & (1-\beta)(\vec{\nabla}W)^c_{ji}.\vec{ij} + \beta(\vec{\nabla}W)^u_{ji}.\vec{ij} \\ & +\xi_c\left[(\vec{\nabla}W)^u_{ji}.\vec{ij} - 2(\vec{\nabla}W)^c_{ji}.\vec{ij} + (\vec{\nabla}W)^d_{ji}.\vec{ij}\right] \\ & +\xi_d\left[(\vec{\nabla}W)_{D^*_{ji}}.\vec{ij} - 2(\vec{\nabla}W)_j.\vec{ij} + (\vec{\nabla}W)_i.\vec{ij}\right] \quad ,\end{aligned} \tag{13}$$

The term $\left(\vec{\nabla}W\right)_{D^*_{ij}}$ is the gradient at the point D^*_{ij}. This last gradient is computed by interpolation of the nodal gradient values at the nodes contained in the face opposite to i in the upwind triangle T_{ij}.

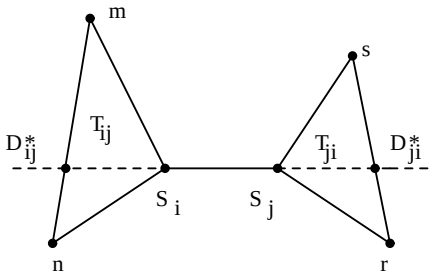

Figure 6: Localisation of the extra interpolation points D^*_{ij} and D^*_{ji} of nodal gradients

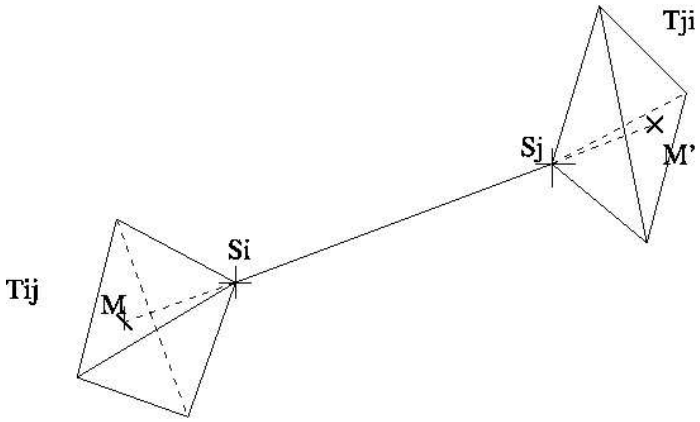

Figure 7: Edge-upwind tetrahedra

The coefficients β, ξ^c and ξ^d are upwinding parameters that control the combination of fully upwind and centered slopes.

	β	ξ^c	ξ^d	δ	Order
β-scheme	1/3	0	0	1	3
β-scheme	1/3	0	0	0	4
Present Method	1/3	-1/30	-2/15	1	5
Present Method	1/3	-1/30	-2/15	0	6

Table 3: Accuracy of different versions of the new scheme in 2D regular case

To sum up, these schemes have only sixth-order dissipation and are in general second-order accurate but they become higher-order accurate in the linear case for some values of the parameters β (see [10]) ξ^c and ξ^d, see [12] and Table 3.

4 Linearisation

The natural model for the propagation of acoustics in a fluid is the compressible Navier-Stokes equations. However their use for this purpose is difficult small amplitude of variation that corresponds to acoustics phenomena.

In that case the linearised Euler model is generally a reasonable one. The Euler equations are denoted by:

$$W_t + F(W)_x + G(W)_y = 0 \tag{14}$$

and their linearisation near a steady flow W_0 writes:

$$W_t + (F'(W_0)W)_x + (G'(W_0)W)_y \;=\; 0\ . \tag{15}$$

In an ideal situation, we wish an approximation of the linearised system that be *conservative* and *non dissipative*. In practice, we need to introduce some dissipation with a Riemann solver.

4.1 Linearisation of a Riemann solver

The interest of a good upwinding is a rather rational way in introducing dissipation. The flux difference splitting proposed by Roe writes:

$$(F(U_L) + F(U_R))/2 \;-\; |A(\tilde{U})|(U_R - U_L)/2 \tag{16}$$

where $\tilde{U}$ holds for the Roe average of U_R and U_L. This average ensures that Roe's splitting is upwind in supersonic case, but this holds only in nonlinear case. A not identical, but very

close, formulation is the following:

$$(F(U_L) + F(U_R))/2 \; - \; sign(A(\tilde{U}))(F(U_R) - F(U_L))/2 \tag{17}$$

in which $sign(A)$ for a diagonalisable matrix $A = T^{-1}\Lambda T$, with $\Lambda = Diag(\lambda_1, \lambda_2, \lambda_3)$ holds for the expression:

$$sign(A) \; = \; T^{-1} Diag(sign(\lambda_1), sign(\lambda_2), sign(\lambda_3))T. \tag{18}$$

We can easily check that this form allows full upwinding if all λ_i are of same sign, this time without assuming that $\tilde{U}$ is the Roe average. As a linearised version, we suggest:

$$(F'(U_L)W_L + F'(U_R)W_R)/2 \; - \; \delta sign(A(\tilde{U}))(F(W_R) - F(W_L)) \tag{19}$$

Where $\tilde{U}$ can be produced by any symmetric averaging. Coefficient δ is to be chosen small, in order to gain benefit of the extra stability of a linear formulation.

4.2 Linearisation and global approximation

We now extend the high-order accurate construction of the first section to the case of variable coefficients. We first start from a 1D scalar case:

$$W_t + (c(x)u(x))_x \; = \; 0. \tag{20}$$

One novelty with respect to [4] and [5], is that we want to save the order of accuracy for a non-uniform background flow, represented here by $c(x)$. Our proposition for this purpose is to apply the high order derivation operators to the *fluxes* $c(x)u(x)$.

This is done by interpolating variable $cu(x)$, from its values $(cu)_i$ on each node, and from its nodal gradients $(\nabla u)_i$. We obtain cell interface values $(cu)^+_{i+1/2}$ and $(cu)^-_{i+1/2}$ at abscissae $x_{i+1/2}$.

The resulting spatially semi-discretized scheme writes:

$$area(i) \; W_{i,t} + \Phi_{i+1/2} \; - \; \Phi_{i-1/2} \; = \; 0 \tag{21}$$

with

$$\Phi_{i+1/2} \; = \; 0.5 \;\; ((cu)^+_{i+1/2} + (cu)^-_{i+1/2}) \tag{22}$$

The above averaging of plus and minus values corresponds to a central differencing formulation ("no Riemann solver"). According to the choice among the above "interpolations parameters", it can be of second to sixth order accuracy. We note in passing that the idea of choosing flux interpolation allows to escape to the second-order limitation advocated by Wu and Wang ([13]) for MUSCL schemes.

4.3 Stabilisation

It can be necessary to stabilise the scheme define in the previous section, especially when non-uniform meshes are used.

As criteria of design for designing the stabilisation terms, we propose the following ones:
(i)- stabilisation is directly governed by the discontinuities produced by the interpolations chosen in the central differenced term
(ii)- stabilisation should allow full upwinding (as far as all characteritics are in the same direction, and the interpolation is also full upwind)
(iii)- since the leading error will be directly governed by the first derivatives of eigenvalues, we do not need to interpolate them in a costly way.

$$\Phi^{upwind}_{i+1/2} \;=\; \Phi_{i+1/2} - D_{i+1/2} \tag{23}$$

with

$$D_{i+1/2} \;=\; 0.5\;\delta\; sign(c_{i+1/2})((cu)^{+}_{i+1/2} - (cu)^{-}_{i+1/2}) \tag{24}$$

where $c_{i+1/2}$ is the simple average $(c_i + c_{i+1})/2$. The coefficient δ will allow a fine tuning of the *spatial* dissipation of the scheme and should be less or equal to 1.

4.4 1D linearised Euler Formulation

The interpolation is now applied to the values of the linearised fluxes $F'(U)W$. Stabilisation is inspired by the Riemann solver proposed below. This results in :

$$\Phi^{upwind}_{i+1/2} \;=\; \Phi_{i+1/2} - D_{i+1/2} \tag{25}$$

with:

$$\Phi_{i+1/2} \;=\; 0.5((F'(U)W)^{+}_{i+1/2} + (F'(U)W)^{-}_{i+1/2}) \tag{26}$$

and:

$$D_{i+1/2} \;=\; 0.5\;\delta\; sign(A_{i+1/2})((F'(U)W)^{+}_{i+1/2} - (F'(U)W)^{-}_{i+1/2}) \tag{27}$$

4.5 2D linearised Euler Formulation

The Euler equations are written in short:

$$w_t \;+\; F(W)_x \;+\; G(W)_y \;=\; 0 \tag{28}$$

or:

$$w_t \;+\; div\mathcal{F} \;=\; 0 \tag{29}$$

Let us denote n_{ij} the integral of the normal vector along the interface between two cells, $Cell_i$ and $Cell_j$.

The interpolation is now applied to the values of the linearised flux vectors in the normal direction $\mathcal{F}'(U)W \ . \ n_{ij}$. This gives:

$$\Phi_{ij}^{upwind} \ = \ \Phi_{ij} - \mathcal{D}_{ij} \tag{30}$$

with:

$$\Phi_{i+1/2} \ = \ 0.5((\mathcal{F}'(U)W)_{ij} \ . \ n_{ij} + (\mathcal{F}'(U)W)_{ji} \ . \ n_{ij}) \tag{31}$$

and:

$$\mathcal{D}_{i+1/2} \ = \ 0.5 \ \delta \ sign(\mathcal{A}_{ij})((\mathcal{F}'(U)W)_{ij} \ . \ n_{ij} - (\mathcal{F}'(U)W)_{ji} \ . \ n_{ij}) \tag{32}$$

where $\mathcal{A}_{ij}$ is defined by:

$$\mathcal{A}_{ij} \ = \ \mathcal{F}'((U_i + U_j)/2) \ . \ n_{ij}. \tag{33}$$

4.6 Summary of the spatial scheme

The global algorithm for computing the fluxes can be summed as follows.

0. A background flow $U \ = \ (\rho, \rho u, \rho v, E)$ and a perturbation $W \ = \ (\delta\rho, \delta(\rho u), \delta(\rho v), \delta E)$, on each vertex of the mesh are given.

1. Compute the linearised fluxes $\bar{F} \ = \ F'(U).W$, $\bar{G} \ = \ G'(U).W$ on each vertex (vertexwise loop).

2. Compute the nodal gradients $\nabla\bar{F}$, $\nabla\bar{G}$ of the linearised fluxes on each vertex (elementwise loop). This is done by applying the nodal gradient formula:

$$(\vec{\nabla}\bar{F})_i \ = \ \frac{1}{aire(C_i)} \sum_{T \in C_i} \frac{aire(T)}{3} \sum_{k \in T} (\bar{F})_k \, \vec{\nabla} \, \Phi_k^T \tag{34}$$

3. Start *edgewise assembly loop*:
compute the extrapolated slopes :

$$\begin{aligned} (\vec{\nabla}\bar{F})_{ij}.\vec{ij} = \quad & (1-\beta)(\vec{\nabla}\bar{F}))_{ij}^{c}.\vec{ij} + \beta(\vec{\nabla}\bar{F}))_{ij}^{u}.\vec{ij} \\ & +\xi_c \left[(\vec{\nabla}\bar{F}))_{ij}^{u}.\vec{ij} - 2(\vec{\nabla}\bar{F}))_{ij}^{c}.\vec{ij} + (\vec{\nabla}\bar{F}))_{ij}^{d}.\vec{ij}\right] \\ & +\xi_d \left[(\vec{\nabla}\bar{F}))_{D_{ij}^*}.\vec{ij} - 2(\vec{\nabla}\bar{F}))_{i}.\vec{ij} + (\vec{\nabla}\bar{F}))_{j}.\vec{ij}\right] \quad , \end{aligned} \tag{35}$$

(and analog for $\vec{\nabla}(\bar{F}(U,V)))_{ij}$.
The central differenced flux is deduced:

$$\Phi_{ij} \ = \ 0.5 \ (\bar{\mathcal{F}}_i + \nabla\bar{\mathcal{F}}_{ij} \ + \ \bar{\mathcal{F}}_j - \nabla\bar{\mathcal{F}}_{ji}) \ . \ n_{ij} \tag{36}$$

in which:

$$\bar{\mathcal{F}} \ = \ (\bar{F}, \bar{G}) \tag{37}$$

4. Evaluate the stabilisation term:

$$\mathcal{D}_{i+1/2} \;=\; 0.5\;\delta\; sign(\mathcal{A}_{ij})((\bar{\mathcal{F}}_{ij}\;.\;n_{ij} - (\bar{\mathcal{F}}_{ji}\;.\;n_{ij}) \tag{38}$$

where $\mathcal{A}_{ij}$ is defined by:

$$\mathcal{A}_{ij} \;=\; (F', G')((U_i + U_j)/2)\;.\;n_{ij}. \tag{39}$$

5. Compute the final edge flux as:

$$\Phi_{ij}^{upwind} \;=\; \Phi_{ij} \;-\; \mathcal{D}_{ij} \tag{40}$$

and add (substract) it to flux assembly at vertex i (j).

4.7 Boundary conditions

Boundary conditions have a crucial influence on the quality of practical acoustic simulations. Non-reflecting boundary conditions are necessary in order to avoid spurious reflecting waves to travel in the computational domain. In this preliminary study, we shall not consider problems with possible reflections, and we shall use in the presented calculations upwind farfield conditions relying on the Steger-Warming flux splitting. In short, fluxes between boundary cell and external medium are computed as follows:

$$\Phi_i^{external} \;=\; A^+(U_i)W_i \;+\; A^-(U_\infty)W_\infty$$

where $A \;=\; \frac{\partial F}{\partial U}\;.\;n$, n being the normal to boundary, U_∞ and W_∞ respectively the background flow and perturbation specified at farfield.

4.8 Time advancing

The time advanging is as for the 1D scheme a Runge-Kutta one, that can be used in the linearised version defined in (8).

5 In three dimensions

5.1 Medians cells

Extension to 3-D of median cells is not complicated. One just have to take as the exchange surface between two vertices of an element, the triangles connecting:

- the middle of the bar linking the considered apices,
- the center of gravity of the faces of the element having this bar as an edge,
- the center of gravity of the element.

By analogy with 2-D, one should rather construct cells as regular as possible when the mesh is non-structured. Then, one would wish the cells be rectangle parallelepipeds centered around the apices when the mesh is the 3-D equivalent to Friedrichs-Keller mesh. First, it is important to definite the shape of the volumetric elements.

5.2 A new tetrahedrization

In 3-D, space is first divided into hexahedra. For sake of simplicity, the case of a Cartesian mesh is considered. Thus, we consider rectangles parallelepipeds (thereafter called *blocks*), whose volumes are $V_0 = \Delta x \times \Delta y \times \Delta z$. It is desirable to end up with tetrahedral elements; thus, one must split these blocks. Let us focus on two divisions considered before. The first (**D1**) minimizes the number of sub-tetrahedra, but generates a big core element, (volume $=V_0/3$), and four peripheral elements (Volume $= V_0/6$). The second division (**D2**) yields two identical prisms, each being subdivided into three tetrahedra. But, in order to take into account the new cells that will be defined, and our ambition to come back to a Finite Differences scheme, a 3-D triangulation identical to the Friedrichs-Keller type mesh in 2-D is proposed.

The proposed division ("**New Generation** Division, or **NGD**) splits the *block* in six identical tetrahedrons, with volumes $V_0/6$, each being the image of its neighbors in a mirror. All these elements have in common a diagonal of the *block*. The coordinates of the tetrahedrons resulting from the three divisions are shown in Figures 10 and 11, depending upon the local numbers of the block vertices. Figures 8 and 9 show the **D1** and **NGD** divisions.

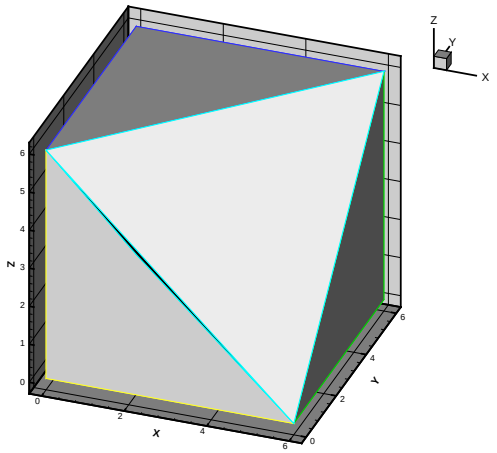

Figure 8: **D1** division

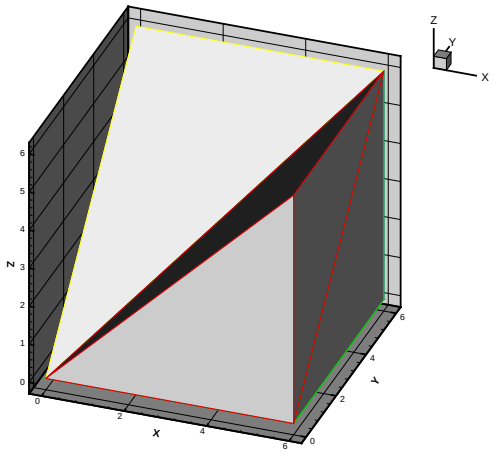

Figure 9: **NGD** division

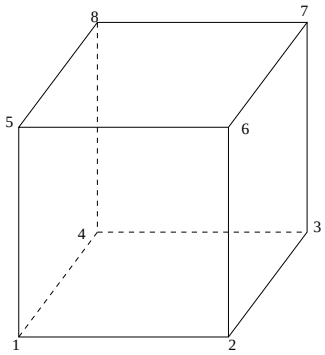

Figure 10: Local numbering of vertices in a *block*

Element	vertices		
	D1	**D2**	**NGD**
1	(2,6,7,5)	(1,2,3,6)	(2,1,4,6)
2	(2,3,4,7)	(1,5,6,7)	(3,2,4,6)
3	(5,8,7,4)	(6,1,7,3)	(7,3,4,6)
4	(1,2,4,5)	(1,5,7,8)	(8,7,4,6)
5	(2,5,7,4)	(1,7,3,8)	(5,8,4,6)
6		(1,3,4,8)	(1,5,4,6)

Figure 11: Sub-tetrahedra vertices identified from local block numbering for the three different splitings

5.3 A new cells generation

One shall name **"New Generation Cells"** (or **NGC**) the group of polyhedrons such that the exchange surface between two neighboring vertices joins, for a given element:

- the middle of the edge connecting these two vertices,
- the **"surface center"** of the faces of the element having this edge in common,
- the "volume center" of the element,

where

- the **"surface center"** of a given face is its c.c.c. if it comprises only acute angles otherwise, it is the closest point of the triangle, i.e. the middle of its longest edge,
- the **"volume center"** of an element is its c.c.s. if the former is located inside the element; otherwise, it is the closest point, i.e. the **"surface center"** of the largest surface.

One can notice that when tetrahedra result from **NGD** then all the elements faces are rectangle triangles. In this case, the cell joins the middle of the longest edge of the tetrahedron to the middles of the other edges. The cells generated in this way are blocks, centered around the vertices of the mesh. Figures 12 and 13 show the trace of the division of an element into cells, according to the old and new methods, respectively.

In first instance, one should point out that the generated cells minimize the numerical dissipation error due to the angles between the perpendicular to the cells and the edges they cross. On the other hand, it can be shown that by **NGD** tetrahedrization and the new cells definitions, it is possible to increase the order of the space scheme. Indeed, using $MUSCL$ with a nodal upwind gradient, defined in the same way as in 2-D in [4], one comes back to

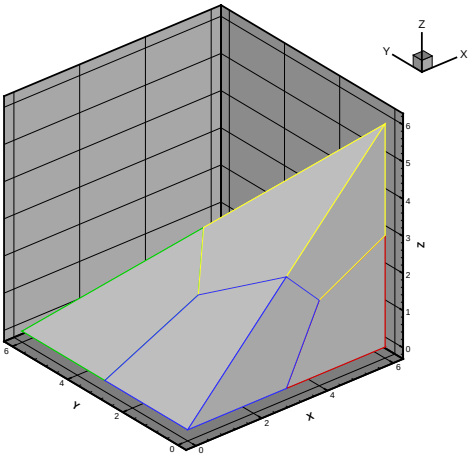

Figure 12: Trace of medians cells on a tetrahedron resulting from **NGD**

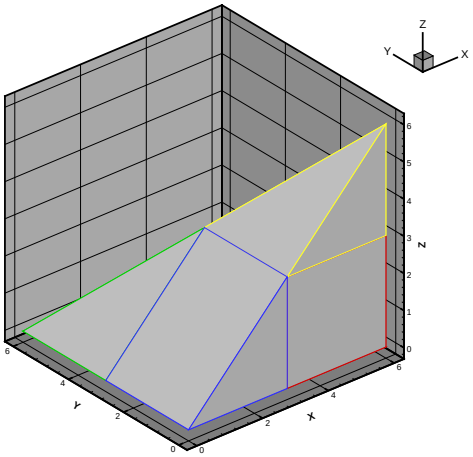

Figure 13: Trace of **NGC** on a tetrahedron resulting from **NGD**

Finite Differences. One can therefore expect to notice an order above 2 (scheme order with the previous division).

6 Numerical experiments in 2D

We shall concentrate on uniform background flow. An example of non-uniform background flow is given in [14] and [15]. The numerical experiments presented here are of two types. Firstly, we check the accuracy order of our schemes. Secondly, we compute a well known test case in order to evaluate their accuracy in a more practical context.

6.1 Accuracy validation

In order to have an analytical context for accuracy validation, we choose a solution which is very small near the boundaries of the computational domain. For realizing this programme, we have to introduce sources terms in our formulation.

6.1.1 Test case description

We define the background flow $\bar{U}$ as:

$$\overline{U} = \begin{pmatrix} 1.0 \\ M_x \\ M_y \\ 1/\gamma \end{pmatrix}.$$

The system of linearized Euler equations with time and space dependent source terms is prescribed as

$$\begin{aligned}
&\frac{\partial \rho}{\partial t} + \frac{\partial (M_x \rho + u)}{\partial x} + \frac{\partial (M_y \rho + v)}{\partial y} = B\omega \cos(\omega\, t) e^{\left(-A\left(x^2+y^2\right)\right)} = \\
&\frac{\partial u}{\partial t} + \frac{\partial (M_x u + p)}{\partial x} + \frac{\partial M_y u}{\partial y} = \\
&B\left(-M_x \omega \cos(\omega\, t) + 2 M_x^2\, A\, x \sin(\omega\, t) - 2\, \sin(\omega\, t)\, A\, x + 2\, M_y\, M_x\, \sin(\omega\, t)\, A\, y\right) e^{\left(-A\left(x^2+y^2\right)\right)} \\
&\frac{\partial v}{\partial t} + \frac{\partial M_x u_+}{\partial x} \frac{\partial (M_y v + p)}{\partial y} = \\
&B\left(-M_y\, \omega\, \cos(\omega\, t) + 2\, M_x\, M_y\, \sin(\omega\, t)\, A\, x + 2\, M_y^2\, \sin(\omega\, t)\, A\, y - 2\, \sin(\omega\, t)\, A\, y\right) e^{\left(-A\left(x^2+y^2\right)\right)} \\
&\frac{\partial p}{\partial t} + \frac{\partial (M_x p + u)}{\partial x} + \frac{\partial (M_y p + v)}{\partial y} = B\omega \cos(\omega\, t) e^{\left(-A\left(x^2+y^2\right)\right)}
\end{aligned} \tag{41}$$

The initial data is taken equal to zero that is

$$\rho(0,x,y) = 0, \quad u(0,x,y) = 0, \quad v(0,x,y) = 0, \quad p(0,x,y) = 0 \tag{42}$$

The resulting initial boundary value problem (41)-(42) has the following analytical solution

$$\begin{aligned}
\rho(x,y,t) &= B \sin(\omega\, t) e^{\left(-A\left(x^2+y^2\right)\right)} \\
u(x,y,t) &= -M_x\, B \sin(\omega\, t) e^{\left(-A\left(x^2+y^2\right)\right)} \\
v(x,y,t) &= -M_y\, B \sin(\omega\, t) e^{\left(-A\left(x^2+y^2\right)\right)} \\
p(x,y,t) &= \rho(x,y,t)\ .
\end{aligned} \tag{43}$$

The particularity of this solution is that it is a function of finite space support. This property is expected to prevent from troubles connected with free boundary conditions.

6.1.2 Modification of time integration procedure

Let us study the time integration of the equations system (41). It is easy to verify that the usual Jameson procedure (8) provides a high order of time approximation only for ordinary linear differential equations of form $dy/dt = \lambda y + at$ (where λ and a are constants) and only the second order for any other right hand side of the ODE.

In a general case including the validation test case, we have the following ordinary differential equations

$$\frac{dU}{dt} = L(U) + f(t) \tag{44}$$

where L is **linear** differential operator and $f(t)$ is the source term **non-linearly dependent on time** t and **independent on the solution** U.

In order to provide high accuracy order, we should modify the Jameson time integration for the case of nonlinear on t source terms. In doing so as usually, let us apply the Taylor expansion of function y defined by the equation (44), replace the corresponding time gradients by their values taken from (44) and rearrange the terms. As a result, the time integration technique can be formulated as the following low storage multi-stage (N-stage) algorithm

$$\begin{aligned}
&U^{(0)} = U^n \\
&U^{(k)} = U^{(0)} + \frac{\Delta t}{N-k+1} L\left(U^{(k-1)}\right) + (N-k)! \sum_{l=1}^{k} \frac{\Delta t^l}{(N-k+l)!} \frac{d^{l-1} f}{dt^{l-1}}, \quad k = 1 \ldots N \\
&U^{n+1} = U^{(N)}
\end{aligned} \tag{45}$$

6.1.3 Numerical results

The test conditions are further specified by choosing $M_x = M_y = 0.5\cos(\pi/4)$ and $A = 0.002$, $B = 0.1$. Two variants are considered. They differ only by the choice of frequency ω in (43) and different final times T_{final}:

- TEST 1: $\omega = 2\pi \times 0.0125$, $T = 2\pi/\omega = 80.$, $T_{final} = 20.$
- TEST 2: $\omega = 2\pi \times 0.1$, $T = 2\pi/\omega = 10.$, $T_{final} = 40.$

The integration has been done both according to the technique (45) and "classical" fourth order Runge-Kutta method with the unique Courant number equal to 0.25.
All the computations have been done on regular meshes (coarse, $\Delta x = \Delta y = 2.$ and fine, $\Delta x = \Delta y = 1.$) with the use of Barth cells.
A study of the computational accuracy is presented with the use of three different norms,

$$\begin{aligned}
\|u\|_C &= \max_{1 \le i \le N} |\rho - \rho^{exact}|, \\
\|u\|_{L_1} &= \sum_{i=1}^{N} |\rho - \rho^{exact}| \, meas(C_i), \\
\|u\|_{L_2} &= \left(\sum_{i=1}^{N} |\rho - \rho^{exact}|^2 \, meas(C_i) \right)^{1/2}
\end{aligned} \tag{46}$$

where $meas(C_i)$ is computed with the Barth cell option. An numerical accuracy order n is calculated by the following formulas

$$n = - \frac{\ln \|\rho - \rho^{exact}\|^{\text{finemesh}} - \ln \|\rho - \rho^{exact}\|^{\text{coarsemesh}}}{\ln(Dx)^{\text{finemesh}} - \ln(Dx)^{\text{coarsemesh}}} \tag{47}$$

We compare first the two test cases with the best scheme, corresponding to $\delta = 0$. In Tables 4 and 5, we get confirmation that this scheme is of sixth order accuracy and its implementation is validated.

	C Error	L1 Error	L2 Error
Coarse	0.908D-07	0.284D-03	0.278D-05
Fine	0.155D-08	0.520D-05	0.457D-07
Numerical order	5.872	5.771	5.927

Table 4: Density errors for $\delta = 0 : \omega = 0.0125 \times 2\pi$, $T = 80$.

	C Error	L1 Error	L2 Error
Coarse	0.207D-07	0.232D-04	0.365D-06
Fine	0.358D-09	0.607D-06	0.823D-08
Numerical order	5.854	5.256	5.471

Table 5: Density errors for $\delta = 0 : \omega = 0.1 \times 2\pi$, $T = 10$.

We added the computation of TEST 1 with the dissipative version, i.e. with $\delta = 1$. Table 6 displays the results that validate the theoretical analysis (fifth order).

Some comments can be made. The main point is that the expected accuracy is verified. We emphasize that this validation does not include the boundary region, since our solution is very small near the boundary. However, the treatment of reflecting wall could with some schemes be computed with high-order accuracy. In our options, the proposed scheme is not able to do this, even with a cartesian mesh. This disadvantage is the result of our design

	C Error	L1 Error	L2 Error
Coarse	0.838D-06	0.269D-02	0.271D-04
Fine	0.264D-07	0.840D-04	0.854D-06
Numerical order	4.988	5.001	4.988

Table 6: Density errors for $\delta = 1 : \omega = 0.0125 \times 2\pi$, $T = 80$.

options, but we recall that our target computation is acoustics in complex geometry and in general the mesh will not be cartesian in the direct vicinity of the walls, but it can be cartesian in the rest of the computational domain.

6.2 Tam test case

A second test case is now considered in order to study the accuracy of the proposed scheme on a more typical acoustic problem. The problem to solve is taken from the *ICASE/LaRC Workshop on Benchmark Problems in Computational Aeroacoustics (CAA)* held in Hampton, Virginia in October 24-26, 1994 ([16]).

6.2.1 Test case formulation

We put again

$$\overline{U} = \begin{pmatrix} 1.0 \\ M_x \\ M_y \\ 1/\gamma \end{pmatrix}$$

and the vector components of initial acoustic disturbances are described as

$$\begin{aligned}
\rho(x,y,0) &= \exp(-\frac{\ln 2}{9}(x^2+y^2)) + 0.1\exp(-\frac{\ln 2}{25}((x-67)^2+y^2)) \\
u(x,y,0) &= 0.04y\exp(-\frac{\ln 2}{25}((x-67)^2+y^2)) \\
v(x,y,0) &= -0.04(x-67)\exp(-\frac{\ln 2}{25}((x-67)^2+y^2)) \\
p(x,y,0) &= \exp(-\frac{\ln 2}{9}(x^2+y^2)).
\end{aligned}$$

This initial boundary value problem has the following analytical solution

$$
\begin{aligned}
u(x,y,t) &= \frac{x - M_x t}{2\frac{\ln 2}{25}\eta} I1 + 0.04(y - M_y t) exp(-\frac{\ln 2}{25}((x - 67 - M_x t)^2 + (y - M_y t)^2)) \\
v(x,y,t) &= \frac{y}{2\frac{\ln 2}{9}\eta} I1 + 0.04(y - M_y t) exp(-\frac{\ln 2}{25}((x - 67 - M_x t)^2 + (y - M_y t)^2)) \\
p(x,y,t) &= \frac{1}{2\frac{\ln 2}{9}} I2 \\
\rho(x,y,t) &= p + 0.1 \exp(-\frac{\ln 2}{25}((x - 67 - M_x t)^2 + y^2))
\end{aligned}
\tag{48}
$$

where

$$
I1(x,y,t) = \int_0^\infty \exp(-\frac{-\xi^2}{4\ln 2})\, J_1(\xi\eta)\xi \sin \xi t \, d\xi
$$

$$
I2(x,y,t) = \int_0^\infty \exp(-\frac{-\xi^2}{4\ln 2})\, J_0(\xi\eta)\xi \cos \xi t \, d\xi
$$

J_0 and J_1 are the corresponding Bessel functions.

6.2.2 Results

The following test cases are considered. In the first test problem (TEST 3) the mean flow velocities are $M_x = 0.5$, $M_y = 0.0$ which corresponds to the case of a 'horizontal wind' from the left. In the second test problem (TEST 4) these velocities are $M_x = 0.5\cos\left(\frac{\pi}{4}\right)$, $M_x = 0.5\cos\left(\frac{\pi}{4}\right)$ which corresponds to a 'diagonal wind' from the left bottom corner of a computational domain. Both problems are solved in a square $x_1 = -100$, $x_2 = 100$, $y_1 = -100$, $y_2 = 100$.

A typical numerical result is represented for the density disturbances in Figure 14. The solution cuts are given at the same fixed time moment $t = 40$.

6.2.3 Some comments on results

The above results lead to the following comments.

	Cartesian mesh Test 4		Unstructured mesh Test 3	
	Coarse mesh 10201 nodes	Fine mesh 40401 nodes	Coarse mesh 9693 nodes	Fine mesh 39527 nodes
MC/$\delta = 1$	9.910×10^{-1}	1.886×10^{-1}	1.019×10^{0}	1.406×10^{-1}
Num.Order	2.393		1.99	
MC/$\delta = 0$	1.202×10^{0}	1.306×10^{-1}	1.245×10^{0}	9.878×10^{-2}
Num.Order	3.202		2.54	
BC/$\delta = 1$	7.927×10^{-1}	1.044×10^{-1}	1.009×10^{0}	1.420×10^{-1}
Num.Order	2.925		1.97	
BC/$\delta = 0$	8.689×10^{-1}	5.217×10^{-2}	1.293×10^{0}	1.797×10^{-1}
Num.Order	4.053		1.98	
Compact-RK(L2)	0.713×10^{0}	0.587×10^{-1}		
Num.Order	3.623			
DRP(L2)	0.473×10^{0}	0.981×10^{-1}		
Num.Order	2.271			

Table 7: Density L2 errors for four versions of the presented scheme, i.e. with dissipation parameter δ set equal to 1 and to 0, and with cell shapes of median type (MC) or of Barth type (BC). The results are compared with the ones of cartesian calculations [17] with the use of fourth-order compact finite-difference and DRP schemes.

- Numerical accuracy order varies from 2.3 to 4., but most of measurements are not fully demonstrative since the results on the coarse meshes involve oscillations.
- The Barth cell option behaves better in the cartesian case and slightly worse in the unstructured case.
- Numerical dissipation improves the solution quality on some coarse meshes but not on all of them.
- The comparison between unstructured meshes and structured ones is possible since test cases 3 and 4 are of equivalent difficulty. It is not so defavourable to the unstructured case. The error on coarse meshes differs generally of only a few pourcents. On the fine meshes, the smallest unstructured error (9.810^{-2}) is not twice larger than the best structured one (5.210^{-2}). In most computation on the unstructured meshes, the oscillations are observed at least on the coarse meshes, but the numerical order of accuracy stays notably larger than 2.
- The test case is rather well computed with the cartesian fine mesh. Our scheme is well compared with the standard schemes for structured or cartesian meshes (DRP scheme [1], compact Runge-Kutta method [17]). We emphasize that none of the schemes that was tried on this case could produce a numerical order of accuracy close to the

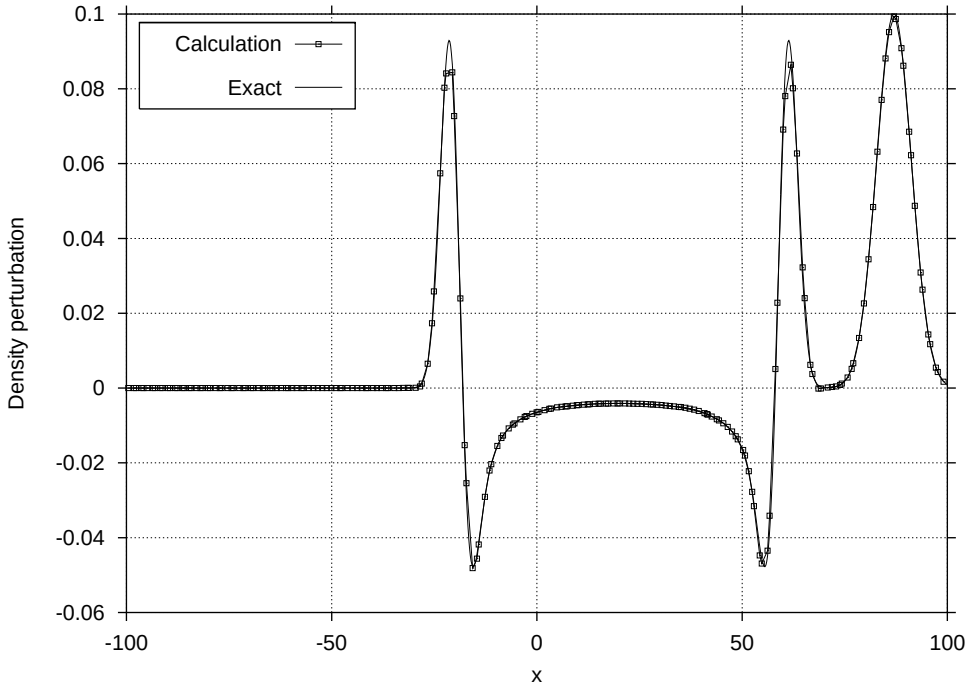

Figure 14: **TEST 4. Acoustic waves in diagonal wind.**
Structured mesh, $\delta = 0$, median cells (40401 nodes)

theoretical one. This is explained by the arising of details in the exact solution that are smaller than the mesh size, at least for the coarse mesh.

- It should be noted that the exact solution is given only as a solution of linearised Euler equations and can not be considered as a physical one. This fact is demonstrated in Figure 15 where the result of using nonlinear Euler model is represented. The choice of mathematical model for the acoustic waves description is very important since even in the case of rather small disturbances the linear models can produce very inaccurate results (see [14], [15]).

7 Numerical experiments in 3D

The test case is the direct adaptation of the case presented in 6.1. We use a unique computational domain for three computations. It is the parallelopiped $[-100, 100] \times [-2, 2] \times [-2, 2]$. Meshes 1,2,3 are defined from mesh sizes $h = 1, 0.5$ and 0.25. In 16 we depict the L^2 numerical order as a function of time for the combination of new cube splitting **NGD** and new

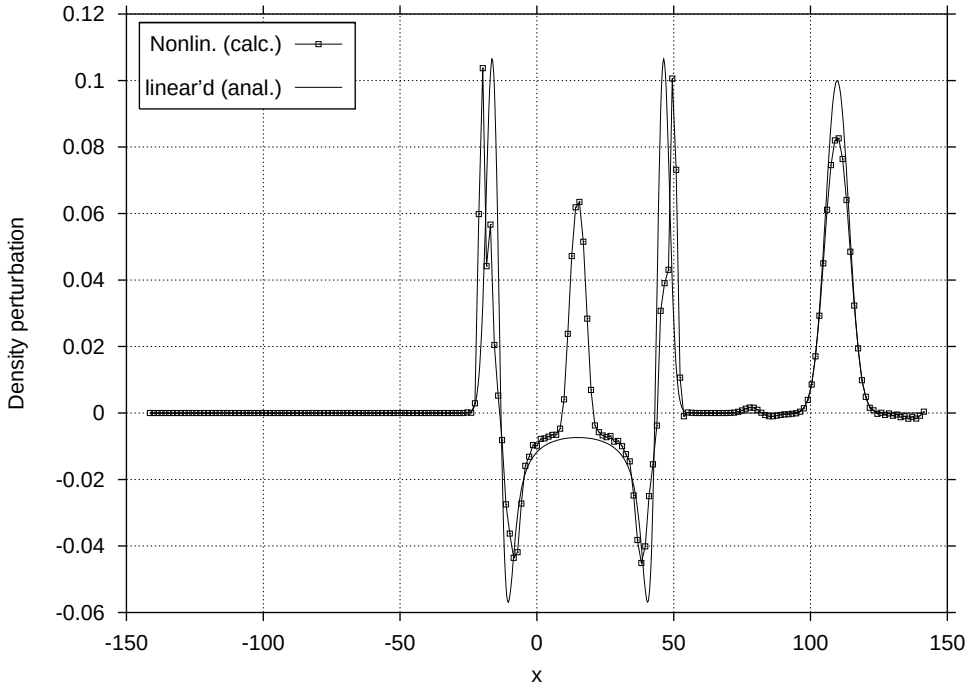

Figure 15: **TEST 4. Comparison between linearised (analytic) solution and nonlinear (approximate) one**

cells **NGC**. After some adaption due to singular starting, the numerical order is confirmed as close to 5.

8 Conclusion

We have proposed a new family of schemes for the linearised Euler equations without or with sources.

The proposed schemes can be applied to unstructured triangulations. They are at least second-order accurate, and involve a tunable small stabilisation term made with a sixth-order derivative. The accuracy is much better that for usual second-order schemes.
The schemes also enjoy superconvergence properties on cartesian meshes, up to a small vicinity of the boundary. Superconvergence order of accuracy can be as high as 5 or 6.

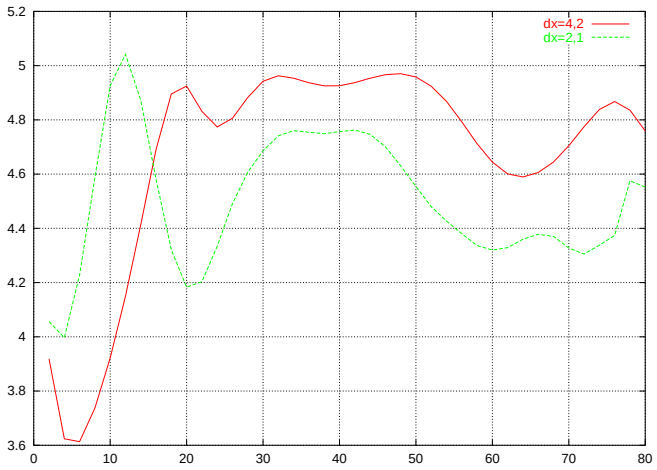

Figure 16: 3D scheme : numerical order as function of time

This order of accuracy is observed for adhoc test cases. For a basic acoustics test case ([16]), the accuracy is good on cartesian meshes and still rather good on unstructured meshes.

Further experiments of the schemes are in progress. In particular, the computation of test case on acoustic waves in non-uniform flows fields is presented in [14], [15].

The proposed schemes appear suitable for the advection parts also with nonlinear fluxes. The same papers ([14], [15]) consider the scheme modification accounting for nonlinear effects in acoustic waves dynamics. A specially elaborated test case is computed. The results show the difference in linear and nonlinear models as well as the possibility of negative influence of round off errors.

References

[1] C. K. W. Tam, J. C. Webb, Dispersion-Relation-Preserving Finite Difference Schemes for Computational Acoustics. *Journal of Computational Physics*, **107**, 261-281, 1993.

[2] R. Abgrall. An essentially non-oscillatory reconstruction procedure on finite element type meshes, application to compressible flows. *Computer Methods in Applied Mechanics and Engineering*, **116**, 1994, 95-101.

[3] F. Bassi and S. Rebay. A high-order accurate discontinuous finite element method for the numerical solution of the compressible Navier-Stokes equations. *Journal of Computational Physics*, **131**, 1997, 267-279.

[4] C. Debiez, A. Dervieux. Mixed Element Volume MUSCL methods with weak viscosity for steady and unsteady flow calculation. *Computer and Fluids*, 1999,**29**, 89-118

[5] C. Debiez, A. Dervieux, K. Mer, and B. NKonga. Computation of unsteady flows with mixed finite/finite element upwind methods. *International Journal for Numerical Methods in Fluids*, 1998, **27**, 193-206.

[6] B. van Leer. Towards the Ultimate Conservative Difference Scheme I. The Quest of Monotonicity, *Lectures notes in Physics*, 1972, **18**, p.163

[7] A. Jameson. Artificial diffusion, upwind biasing, limiters and their effect on accuracy and multigrid convergence in transonic and hypersonic flows. *AIAA paper 93-3359*. AIAA 11th Computational Fluid Dynamics Conference, Orlando, FL,1993.

[8] A. Dervieux. Steady Euler Simulations Using Unstructured Meshes. Von Karman Institute for Fluid Dynamics, Lecture series 1985-04, Computational Fluid Dynamics (1985). Revised version published as a chapter of "Partial Differential Equations of hyperbolique type and Applications", Geymonat Ed., World Scientific, Singapore, 1987.

[9] T. Barth. Aspects of Unstructured Grids and Finite-Volume Solvers for the Euler and Navier-Stokes Equations, in *Special Course on Unstructured Grid Methods for Advection Dominated Flows, AGARD report 787*, p. 6-1 to 6-61, 1992.

[10] J-A. Desideri, A. Goudjo, and V. Selmin. Third-order numerical schemes for hyperbolic problems. *Research report INRIA, No. 607*, 1987.

[11] I. Abalakin, A. Dervieux, and T. Kozubskaya, A vertex centered high order MUSCL scheme applying to linearised Euler acoustics. *Research report INRIA, No. 4459*, 2002.

[12] R. Carpentier. *Approximation d'écoulements instationnaires. Application à des instabilités tourbillonnaires.* Thesis, University of Nice-Sophia Antipolis, 1995.

[13] H. Wu and L. Wang. Non-existence of third order accurate semi-discrete MUSCL-type schemes for nonlinear conservation laws and unified construction of high accurate ENO schemes. *Sixth International Symposium on Computational Fluid Dynamics*, September 4-8, 1995, Lake Tahoe, NV.

[14] I. Abalakin, A. Dervieux, T. Kozubskaya. Computational Study of Mathematical Models for Noise DNS, *AIAA paper* 2002-2585

[15] I. Abalakin, A. Dervieux, T. Kozubskaya. High Accuracy Study of Mathematical Models for DNS of Noise around Steady Mean Flow, in Proc. of *West East High Speed Flow Field Conference 2002*, D.E. Zeitoun, J. Periaux, J.A. Desideri, M. Marini (Eds.), CIMNE, Barcelona (2002)

[16] "ICASE/LaRC Workshop on Benchmark Problems in Computational Aeroacoustics(CAA)", NASA Conference Publication, Hampton, Virginia, October 24-26, 1994.

[17] I. Abalakin, V. Bobkov, A. Dervieux, T. Kozubskaya, V. Shiryaev, Study of high accuracy order schemes and non-reflecting boundary conditions for noise propagation problems, Liapunov Institute report, project 99-02, 2001, available on : http://www-sop.inria.fr/tropics/Alain.Dervieux/liapunov.html

[18] I. Abalakin, A. Dervieux, T. Kozubskaya. On accuracy of noise direct calculation based on Euler model, *Int. J. Acoustics*(to appear).

[19] Stéphane Lemaire, Gilbert Rogé. Aéroacoustique appliquée aux avions d'affaires: Problématique, méthodologie et outils envisagés chez Dassault Aviation (in french) *38ème colloque d'aérodynamique appliquée Aéroacoustique des véhicules aéronautiques et terrestres, AAAF*, Arcachon 7-9 octobre 2002,

[20] S. Camarri, M.V. Salvetti, B. Koobus, A. Dervieux. Numerical diffusion based on high-order derivatives in MUSCL schemes for LES on unstructured grids, in the proceedings of *DLES-4, Direct and Large-Eddy Simulation-IV*, July 18-20,2001, Twente (Holland)

[21] S. Camarri, M.-V. Salvetti, A. Dervieux, B. Koobus. A low diffusion MUSCL scheme for LES on unstructured grids, *Research report INRIA, No. 4412*, July 2002

[22] S. Camarri, B. Koobus, M.V. Salvetti, A. Dervieux. A low-diffusion MUSCL scheme for LES on unstructured grids. *Computers and Fluids* (to appear)

Unité de recherche INRIA Sophia Antipolis
2004, route des Lucioles - BP 93 - 06902 Sophia Antipolis Cedex (France)

Unité de recherche INRIA Futurs : Parc Club Orsay Université - ZAC des Vignes
4, rue Jacques Monod - 91893 ORSAY Cedex (France)
Unité de recherche INRIA Lorraine : LORIA, Technopôle de Nancy-Brabois - Campus scientifique
615, rue du Jardin Botanique - BP 101 - 54602 Villers-lès-Nancy Cedex (France)
Unité de recherche INRIA Rennes : IRISA, Campus universitaire de Beaulieu - 35042 Rennes Cedex (France)
Unité de recherche INRIA Rhône-Alpes : 655, avenue de l'Europe - 38334 Montbonnot Saint-Ismier (France)
Unité de recherche INRIA Rocquencourt : Domaine de Voluceau - Rocquencourt - BP 105 - 78153 Le Chesnay Cedex (France)

Éditeur
INRIA - Domaine de Voluceau - Rocquencourt, BP 105 - 78153 Le Chesnay Cedex (France)
http://www.inria.fr
ISSN 0249-6399